

# Mapping ultrafast timing jitter in dispersion-managed 89 GHz frequency microcombs via self-heterodyne linear interferometry

Wenting Wang<sup>1,\*†</sup>, Hao Liu<sup>1,†</sup>, Jinghui Yang<sup>1</sup>, Abhinav Kumar Vinod<sup>1</sup>, Jinkang Lim<sup>1</sup>, Yoon-Soo Jang<sup>1</sup>, Heng Zhou<sup>2</sup>, Mingbin Yu<sup>3,4</sup>, Patrick Guo-Qiang Lo<sup>3,5</sup>, Dim-Lee Kwong<sup>3</sup>, Peter DeVore<sup>6</sup>, Jason Chou<sup>6</sup>, and Chee Wei Wong<sup>1,\*</sup>

<sup>1</sup> Fang Lu Mesoscopic Optics and Quantum Electronics Laboratory, University of California, Los Angeles, CA 90095, United States of America

<sup>2</sup> Key Lab of Optical Fiber Sensing and Communication Networks, University of Electronic Science and Technology of China, Chengdu 611731, China

<sup>3</sup> Institute of Microelectronics, A\*STAR, Singapore 117865, Singapore

<sup>4</sup> State Key Laboratory of Functional Materials for Informatics, Shanghai Institute of Microsystem and Information Technology, and Shanghai Industrial Technology Research Institute, Shanghai, China

<sup>5</sup> Advanced Micro Foundry, Singapore 117685, Singapore

<sup>6</sup> Lawrence Livermore National Laboratory, Livermore, CA 94550, United States of America

† These authors contributed equally to this work.

\* To whom correspondence should be addressed. Email: wentingwang@ucla.edu;

cheewei.wong@ucla.edu

**Laser frequency microcombs provide equidistant coherent frequency markers over a broad spectrum, enabling new frontiers in chip-scale frequency metrology, laser spectroscopy, dense optical communications, precision distance metrology and astronomy. Here we demonstrate thermally stabilized frequency microcomb formation in dispersion-managed microresonators at the different mode-locking states featured with the negligible center frequency shift and broad frequency bandwidth. Subsequently, femtosecond timing jitter in the microcombs are characterized, supported by precision metrology on the timing phase, relative intensity noise and instantaneous linewidth. We contrast the fundamental noise for a range of 89 GHz microcomb states, from soliton crystals to multiple solitons and single-soliton regimes, determined by pump-resonance detuning. For the single-soliton state, we report a close-to-shot-noise-limited relative intensity noise of -153.2 dB/Hz and a quantum-noise-limited timing jitter power spectral density of 0.4 as<sup>2</sup>/Hz, at 100 kHz offset**

**frequency. This is enabled by a self-heterodyne linear interferometer with 94.2 zs/Hz<sup>1/2</sup> timing resolution, 50.6 mHz/Hz<sup>1/2</sup> RF frequency resolution, and 6.7  $\mu$ V/Hz frequency discrimination sensitivity. We achieve an integrated timing jitter at  $1.7 \pm 0.07$  fs, integrated from 10 kHz to 1 MHz. Measuring and understanding the fundamental noise parameters in these high-clock-rate frequency microcombs are essential to advance soliton physics and precision microwave-optical clockwork.**

Laser frequency combs have impacted science and technology fields with their equidistant frequency spacings, serving as unique coherent microwave and optical clockwork [1,2]. Recent emerging applications include, for example, optical clocks for space-borne networks [3,4], precise laser ranging metrology for autonomous platforms [5] and low phase noise radio frequency generation [6, 7], aided by the low timing jitter and coherent control in the mode-locked frequency combs. The observations of dissipative soliton microcombs in single microresonator [8,9] or a coupled-microresonator [10] with smooth spectral profile and dispersive waves [11] offer an opportunity to examine the soliton comb dynamics in miniature platforms. There has been significant progress of the soliton microcomb formation in different nonlinear integrated microresonators such as, Si<sub>3</sub>N<sub>4</sub> [12], AlN [13], LiNbO<sub>3</sub> [14], and AlGaAs [15], benefiting from either ultrahigh quality factors or large nonlinear coefficients. In contrast to bright solitons, dark solitons [16], mode-locked pulses [17], and flat-top pulses [18-20], microcombs can be formed in normal dispersion microresonators with the assistance of mode-crossing-induced frequency shift or self-injection locking, to achieve high pump-to-comb power conversion efficiency and better spectral flatness [21]. The recent demonstration of the electrically pumped turn-key soliton microcomb [22-24] and the mode-locked microcomb [25] further reinforce the viability of the fully integrated frequency microcombs and pave the way for integrated functionalities such as terabit-per-second coherent transceivers [26-28], parallel coherent LiDAR [29], precision frequency metrology and control [30, 31], astrophysical spectrographs [32, 33], laser spectroscopy [34-36], distance ranging [37-39], low-noise microwave generation [40-42], and convolutional processing networks [43, 44].

In soliton microcombs, the pump-resonance detuning noise [45] plays a critical role in the noise transduction via thermo-optic effects or the detuning-dependent soliton self-frequency shift [46]. A “quiet point” exists at a detuning where the dispersive-wave recoil can induce a reduction of the impact of the Raman-induced soliton self-frequency shift, suppressing the detuning noise

transduction to the repetition rate phase noise [47]. The noise of the soliton microcomb can be improved after accessing the quiet regime [45, 48], utilizing the cavity mode injection locking [25], intracavity Brillouin-laser pumping [49], optimizing high-order dispersion [50], and suppressing thermorefractive noise with thermal cooling [51]. Furthermore, quantum diffusion has also been observed recently in counter-propagating soliton pairs after technical noise suppression to explore the quantum-noise-limited timing jitter [52] and a photonic fiber-based flywheel at the quantum-noise limit has been realized [53]. The demonstrated microcombs usually suffer from significant Raman-induced center frequency shift, soliton recoil from the mode-crossing frequency shift as well as higher order dispersion, and large cavity group velocity dispersion (GVD). Although the noise performance can be optimized through controlling the linear or nonlinear effects, it is more desirable to avoid the effects. With close-to-zero net GVD, dispersion-managed (DM) soliton microcombs as a distinct modality have been theoretically and experimentally investigated in Kerr active resonators featuring the possibility of a shorter pulse duration as well as better timing stability [54, 55].

Here we demonstrated a series of thermally stabilized microcombs in different mode-locked states in 89 GHz dispersion-managed  $\text{Si}_3\text{N}_4$  microresonators with the negligible center frequency shift and broad frequency bandwidth. The demonstrated DM-microcombs not only expand the scope of soliton physics [8-11], but also provide the possibility to generate low-jitter soliton trains. Subsequently, we determine the intensity fluctuations, timing fluctuations and optical frequency fluctuations of the soliton microcombs and investigate the microcomb noise when operating in the single-soliton state, the multiple soliton state, and the soliton crystal state. Since the microcomb oscillators have high repetition rates (tens of GHz to 1 THz), comparatively low pulse energy, high pulse background, and varied repetition rates from the cavity design, we present a linear interferometry approach with zeptosecond timing jitter resolution to characterize its jitter. We note that the approach [56] is reference-free and independent of the repetition rate, enabling the 89 GHz pulse train timing jitter measurements. The approach is extended recently to characterize timing jitter of the silica microresonator frequency microcomb [42]. The measurement of the fundamental timing jitter is based on: (1) time delay for the frequency discrimination and (2) optical carrier interference for the optical phase discrimination. We observe a relatively intensity noise (RIN) of -153.2 dB/Hz at 100 kHz offset, with a corresponding integrated RIN of 0.034 % from 100 Hz to 10 MHz for the single-soliton pulse. The measured short-term linewidth of the individual comb

lines is 2.3 kHz. For the single-soliton state, the quantum-noise-limited timing jitter PSD is determined at  $0.4 \text{ as}^2/\text{Hz}$  for 100 kHz offset, with an integrated jitter of  $1.7 \pm 0.07 \text{ fs}$  from 10 kHz to 1 MHz, which bodes well for chip-scale optical-microwave clockwork, distributed timing standards, and precision metrology.

### Dispersion-managed microcomb formation

Figure 1a shows the schematic illustration of the dispersion-managed (DM) soliton microcomb formation in the tapered microresonator which includes the scanning electron microscope image of the stoichiometric silicon nitride microresonator with  $261 \text{ }\mu\text{m}$  outer radius and  $800 \text{ nm}$  thickness. The nitride waveguide width is continuously tuned from  $1$  to  $4 \text{ }\mu\text{m}$  to fine-tune the dispersion in the single-mode microresonator. The COMSOL modeled group velocity dispersion (GVD) varies along the microresonator from  $-55$  to  $58 \text{ fs}^2/\text{mm}$  as shown in Figure 1b considering both geometric dispersion and material dispersion. Figure 1c shows the representatively calculated GVD along with the cavity-path averaged GVD with the relation  $\beta_{2\Sigma} = \int \beta_2 dL / L_{cavity}$  where  $\beta_2$  is the GVD of a discrete waveguide segment, and  $L_{cavity}$  is the cavity circumference. The fundamental transverse electric mode features the small anomalous path averaged GVD of  $-3.51 \text{ fs}^2/\text{mm}$  at a pump wavelength of  $1602 \text{ nm}$ . Swept-wavelength interferometry subsequently characterizes the cold cavity dispersion while unveiling its near-single-mode characteristic. The measured free spectral range is  $\approx 89 \text{ GHz}$  with an anomalous group velocity dispersion  $\beta_{2\Sigma}$  of  $-4.39 \text{ fs}^2/\text{mm}$ . The measured loaded and intrinsic quality factor  $Q$ s are  $1.8 \times 10^6$  and  $3.4 \times 10^6$ , respectively.

Subsequently, DM microcombs are generated in the microresonator. Figure 1e illustrates the optical spectrum of the single-soliton DM-microcomb along with the Lugiato-Lefever equation (LLE) modeled spectral profile. Modest spectral dips in the comb spectra, from dispersion discontinuity at two hybridized inter-polarization mode coupling points of  $\approx 1592.64 \text{ nm}$  and  $1659.72 \text{ nm}$ , are observed. The  $1563.64\text{-nm}$  peak is the auxiliary pump laser. To illustrate the temporal dynamics of the microcomb, we measured the intensity autocorrelation (AC) trace with a non-collinear second-harmonic autocorrelator after pump suppression with a bandpass filter. Figure 1f shows the measured pulse width of the single-soliton at  $\approx 305 \text{ fs}$  for the filtered optical spectrum, along with the  $\approx 11.2 \text{ ps}$  ( $1/89\text{-GHz}$ ) pulse train. The measured and modeled pulse duration of the single-soliton is in the inset of Figure 1f. We also observed double-soliton and soliton crystal states in the microresonator. The corresponding optical spectra of the double-soliton

and soliton crystal with one defect are illustrated in Figure 1g and 1i along with the LLE modeled spectral profiles, respectively. The measured optical spectrum of the soliton crystal indicates the destructive interference between a single-soliton microcomb and a  $12 \times$  FSR perfect soliton crystal microcomb. The spatiotemporal LLE modeled intracavity waveforms are depicted in Figure 1h and 1j where single vacancy in the time domain is presented.

### **Relative intensity noise measurement of the dispersion-managed microcombs**

To achieve the DM-microcombs reliably and deterministically, Figure 2a illustrates the implemented TE-TM dual-driven dual-polarization pump approach (more details in Supplementary Information Section I). The forward-propagating pump laser is amplified and selected into the transverse-electric (TE) polarization while the backward-propagating transverse-magnetic (TM) polarized auxiliary laser passively stabilizes the microresonator thermally. Operating effectively in the red-detuned region of one of resonant modes at frequency  $\nu_\mu = c/1602 \text{ nm}$ , we generate the microcombs in a planar tapered dispersion-managed  $\text{Si}_3\text{N}_4$  microresonator through this dual-driven approach based on dynamically photothermal stabilization. The auxiliary laser is blue-detuned from the resonant mode  $\nu_{\mu+53}$  in the reverse direction with the orthogonal polarization direction to mitigate thermal transients during the transition from a high-noise chaotic state to a low-noise mode-locking state and stabilize the pump-resonance detuning thermally. Moreover, the TM-polarized auxiliary laser experiences the normal group-velocity dispersion to avoid the initiation of parametric oscillation. To understand the soliton microcomb performance, we conduct intensity noise, and comb line linewidth measurements of the different soliton microcombs states prior to the respective timing jitter evaluations. Coherence of the soliton frequency combs is examined via the RF intensity noise spectra over a microwave frequency span that is a few times of the cold cavity resonance linewidth. While this distinguishes between the high- and low-noise comb states, it does not identify the noise types nor sources.

To supplement the RF intensity noise measurements of the solitons and soliton crystals, measurement of the relative intensity noise (RIN) is next performed. A signal source analyzer records the intensity fluctuation PSD of the mode-locked pulse train after suppressing the pump laser and careful ensuring the input power does not saturate the low-noise photodetector (detailed in Methods). The representatively filtered optical spectrum is shown as in Figure 2b. The measured

RIN PSD [ $S_{RIN}(f)$ ] of the 89 GHz mode-locked microcombs, normalizing the measured intensity fluctuation PSD [ $S_{\Delta V}(f)$  in units of  $V^2/\text{Hz}$ ] by the average detected power  $|V_0|^2$ , is shown in Figure 2c to 2e corresponding to the single-soliton, double-soliton, and soliton-crystal with one defect microcombs. The gray curves in Figure 2c are the RIN PSD of the spatiotemporal chaotic state [corresponding optical spectra is illustrated in Supplementary Information Section I, Figure S1b<sub>2</sub>] and the pump laser to indicate the upper and lower bounds of the soliton pulse RIN PSD. The soliton microcomb RIN PSD drops with a 30-dB/decade slope ( $1/f^3$ ) over the first offset frequency decade while the cw pump laser RIN PSD falls with a 20-dB/decade slope ( $1/f^2$ ). The discrepancy between two slopes is attributed to external noise sources such as free-space-to-chip coupling fluctuation. For the single-soliton state, the measured RIN is at -153.2 dB/Hz at 100 kHz offset, with a corresponding integrated RIN of 0.034% when integrated from 100 Hz to 10 MHz with the relation of  $RIN_{in} = \int_{f_1}^{f_2} S_{RIN}(f) df$  where  $f_1$  and  $f_2$  are the lower and upper offset frequency bounds. The measured RIN of the double-soliton state and the soliton crystal state are at -149.8 dB/Hz and -148.6 dB/Hz respectively for a 100 kHz offset. The corresponding integrated RIN are 0.036% and 0.023% over the same integrated frequency range. The inset of the Figure 2c shows the electrical noise suppression by optimizing the incident power of the photodetector to facilitate the observation of the dynamical intensity noise of the microcombs. The insets of the Figure 2d and 2e show the noise degradation of the double-soliton and soliton crystal microcombs which are attributed to the conversion of the phase fluctuations to intensity fluctuations in the spectral interference process.

### **Interferometry coherence envelope measurements of soliton microcomb instantaneous linewidths**

To further elucidate the noise characteristics of the soliton microcombs, here we investigate instantaneous linewidths of the generated individual comb teeth and soliton microcomb linewidth distributions. We built a short-time delayed linear interferometer (SDLI) based on Michelson interferometry with a heterodyne detection as shown in Figure 3a. This approach converts the frequency fluctuation [ $\Delta\nu_m = \Delta(f_p + mf_R) = \Delta f_p (1 + m \times \Delta f_R / \Delta f_p)$ ] of the microcomb lines into the second-peak and second-trough (SPST) power contrast difference ( $\Delta P$ ) of the coherent interference pattern in the SDLI. The power spectrum of the SDLI is  $P(f, \Delta f) = P_1 P_2$ , where  $P_1$  is the Lorentzian spectrum and  $P_2$  is the periodic modulation power spectrum. The  $\Delta P$  can be expressed as [57]:

$$\Delta P = 10\log_{10}P_{peak} - 10\log_{10}P_{trough} = 10\log_{10} \frac{[1+(\frac{2}{n_0\Delta\nu\tau})^2][1+\exp(-2\pi n_0\Delta\nu\tau)]}{[1+(\frac{3}{2n_0\Delta\nu\tau})^2][1-\exp(-2\pi n_0\Delta\nu\tau)]} \quad (1)$$

where  $\tau$  is the delay time,  $n_0$  is the refractive index of the fiber, and  $\Delta\nu$  is the comb mode linewidth. Figure 3b shows the measured interferometric coherence envelope of the pump laser and one of comb lines with mode number  $\mu = 44$ , away from the pump. Polynomial curve fitting is used to detect the peak and dip of the interference envelope. Figure 3c shows the measured and calculated interferometric envelope at the different delay time to evaluate the spectral resolution and power dynamic range. The measured linewidth of the pump laser is 1.5 kHz when the delay time is 3.55  $\mu$ s. The corresponding linewidths of the soliton microcomb lines are 2.3 kHz, 3.0 kHz and 2.4 kHz for the single-soliton, double-soliton, and soliton crystal states, as shown in Figure 3d<sub>1</sub>, 3d<sub>2</sub> and 3d<sub>3</sub> at the same delay time along with the modeled interferometric envelopes.

Next, we examine the linewidth distribution of comb lines over the C-band from 1560 nm to 1570 nm to examine linewidth multiplication away from the pump in soliton frequency microcombs. Figure 3e shows the linewidth distribution for the different microcomb dynamical states, with pump centered at  $\approx 1602$  nm and in the range of  $\approx 10$  nm. A slight increase in linewidth further away from the pump towards to shorter wavelength is observed. The linewidth distribution is related to the unbounded timing jitter of the microcombs. In the soliton crystal state, the linewidth distribution has a larger fluctuation which arises from the structured optical spectrum as shown in Figure 1i owing to signal-to-noise ratio dependence of the measurement.

### **Self-heterodyne linear interferometry (HLI) for soliton microcomb femtosecond jitter metrology**

Encouraged by the low RIN and coherent linewidth measurements of the soliton microcombs, we next examine the timing jitter via a self-heterodyne linear interferometer [56]. Figure 4a illustrates the implemented self-heterodyne linear interferometry architecture for the precision timing jitter metrology. The interferometer consists of a reference arm and a time-delayed arm in which a fiber-coupled acousto-optic modulator (AOM) driven by a RF signal  $f_m$  allows heterodyne detection of the phase fluctuation power spectral density (PSD,  $S_\phi$  [dBrad<sup>2</sup>/Hz]). A diffractive grating-based narrowband filter pair selects two modes of the frequency comb at frequencies  $\nu_n = n \times f_R + f_{CEO}$  and  $\nu_m = m \times f_R + f_{CEO}$  as illustrated in the inset of Figure 4a separated by a  $(m-n) \times f_R$  frequency difference where  $f_R$  is the repetition rate and  $f_{CEO}$  is the carrier envelope offset frequency

of the microcombs. Frequency noise  $\Delta\nu(f)$  of the selected modes is subsequently discriminated with delay time  $\tau$  by the relation  $\Delta\phi(f) = 2\pi\Delta\nu(f)\tau$ . The optical phase fluctuations  $\Delta\phi(f)$  are converted into optical intensity fluctuations by linear optical interferometry. At the fiber interferometer output, the two optical modes are demodulated by two photodetectors. The residual phase noise PSD originates from the frequency difference  $(m - n) \times f_R$  of the two selected comb modes, proportional to delay time  $\tau$ . A double-balanced mixer is thereafter used to extract the timing jitter PSD and eliminate the common-mode noise induced by the carrier envelope offset signal and the driven microwave frequency signal ( $f_m$ ). The frequency fluctuations of the two selected optical comb modes are converted into voltage fluctuations with the relation  $\Delta V(f) \propto K_\phi \frac{|1 - e^{-i2\pi f\tau}|}{|i \times f|} (m - n)\Delta f_R(f)$  where  $K_\phi$  is the peak voltage at the double-balanced mixer output. The transfer model shows that the measured voltage fluctuation is proportional to  $|1 - e^{-i2\pi f\tau}|/|i \times f|$ , which implies the output voltage transfer function will have null points at the offset frequency  $f = 1/\tau$  and its harmonics which provides the upper Fourier frequency limit of the timing jitter measurement. The measured voltage fluctuation PSD is subsequently converted into the frequency noise PSD and further into the timing jitter PSD  $S_{\Delta T_R}(f)$  with the relation  $S_{\Delta T_R}(f) = \left(\frac{1}{2\pi f_R}\right)^2 \frac{1}{(m-n)^2} \frac{1}{f^2} \frac{|i \times f|}{K_\phi |1 - e^{-i2\pi f\tau}|} S_{\Delta V}(f)$ . The detected voltage fluctuation at the mixer output is separated into two parts. The first part feedback stabilizes the fiber delay line to avoid free walk, between the optical carrier and fiber interferometer, via a piezoelectric-transduced fiber stretcher (FS) through a loop filter with 1 kHz bandwidth. The second part is recorded by a signal source analyzer which gives the timing fluctuation PSD or a frequency fluctuation PSD of the pulse train envelope. To precisely remove the common-mode noise resulting from dispersion and increase the interferometer signal-to-noise ratio, we utilize a delay control unit (DCU) which contains a motorized fiber delay line (MDL) and a pair of wavelength-division multiplexed (WDM) couplers. One can consider this timing-stabilized and dispersion-compensated fiber link as a true time delay, an optical equivalent of the delay-line frequency discriminator in microwave metrology, to measure the microcomb timing jitter.

We convert the measured voltage fluctuation PSD on the baseband into the repetition rate frequency noise  $S_{\Delta f_R}$  PSD to examine the frequency noise behavior as shown in Figure 4b<sub>1</sub>, 4b<sub>2</sub>, and 4b<sub>3</sub> of the soliton microcomb at the single-soliton, double-soliton, and soliton crystal states. The measured repetition rate frequency noise PSD are 2556 mHz<sup>2</sup>/Hz, 4151 mHz<sup>2</sup>/Hz and, 4168



mHz<sup>2</sup>/Hz respectively at 100 kHz offset. The measured repetition rate frequency noise features the 64 mHz/Hz<sup>1/2</sup> frequency resolution for the single-soliton microcomb. We observe, below  $\approx 20$  kHz frequency offset, the repetition rate frequency noise features a 20-dB/decade slope indicating the repetition rate random walk frequency noise. Based on the power-law, soliton microcombs have a flicker frequency walk of the repetition rate from  $\approx 20$  kHz to 40 kHz offset, a white frequency noise from  $\approx 40$  kHz to 200 kHz offset, and a flicker and white phase noise from  $\approx 200$  kHz to 1 MHz. The resulting integrated linewidths of the free-running repetition rate tone are shown in Figure 4b, for the three microcomb dynamical states.

Figure 4c<sub>1</sub>, 4c<sub>2</sub>, and 4c<sub>3</sub> show the measured timing jitter PSD for the different soliton dynamical states. For the single-soliton comb, the measured quantum-noise-limited timing jitter PSD is 0.4 as<sup>2</sup>/Hz at 100 kHz offset. The corresponding integrated timing jitter is  $1.7 \pm 0.07$  fs when integrated from 10 kHz to 1 MHz as shown in the Figure 4c<sub>1</sub> which is close to the timing jitter in silica microresonator frequency microcomb measured with the similar technology [42]. The achieved femtosecond-level jitter is enabled by the close-to-zero intracavity dispersion to minimize the group delay fluctuations, suppressed nonlinearity with the tapered waveguide, and the thermally stabilized dual-driven soliton formation approach. The quantum-noise-limited timing jitter PSD of the two (double-soliton and soliton crystal) states at 100 kHz offset are at 0.66 as<sup>2</sup>/Hz and 0.82 as<sup>2</sup>/Hz, respectively. This corresponds to an integrated jitter of  $1.9 \pm 0.06$  fs and  $1.8 \pm 0.09$  fs. The measured timing error can be transformed into a timing phase error by  $\Delta\phi_R(f) = 2\pi f_R \times \Delta T_R(f)$ . The dynamical noise is observed in the timing jitter PSD of the soliton crystal microcomb at the offset frequency around 8 MHz. Compared to the direct photon detection for a timing jitter PSD measurement [12, 40, 41], the self-heterodyne linear interferometry can effectively avoid the intensity-noise-to-phase-noise (IM-PM) conversion and the shot-noise limit.

For each of the microcavity soliton states, we observe that the timing jitter PSD drops with a 40-dB/decade slope within 3 to 20 kHz as shown in Figure 4c. Deviation of timing jitter PSD over low Fourier frequency is attributed to the intracavity power fluctuation leading to a  $1/f^4$  slope with the relation of  $S_{\Delta T_R}^{T_R}(f) = \left(\frac{1}{2\pi f T_R}\right)^2 S_{T_R}(f)$  where intracavity power-induced round-trip fluctuations  $S_{T_R} \propto f^{-2}$ . Figure 4c also plots the theoretical cavity thermal bounds on the timing jitter PSD with the yellow solid line, arising from thermorefractive variation and bounding the measured timing jitter PSD from 20 kHz to 40 kHz with a 25-dB/decade slope ( $1/f^{2.5}$ ). In the DM

microresonator, the thermal-noise limited timing jitter PSD, originating from the thermodynamic fluctuations  $\langle \delta T^2 \rangle = k_B T^2 / CV_\mu \rho$  where  $V_\mu$  is the  $\mu$ -th optical mode volume, is described with the model [58]

$$S_{\Delta T_R}(f) = \frac{1}{(2\pi f_R)^2} \left( \frac{v_c}{f_R} \frac{1}{n_0} \frac{dn}{dT} \right)^2 \frac{1}{f^2} \frac{k_B T^2}{\sqrt{2\pi^4 \kappa \rho C f}} \frac{1}{R \sqrt{d_r^2 - d_z^2}} \frac{1}{[1 + (2\pi f \tau_d)^{3/4}]^2} \quad (2)$$

where  $dn/dT$  is the thermorefractive coefficient,  $k_B$  is Boltzmann constant,  $T$  is the chip operating temperature,  $\kappa$  is thermal conductivity,  $\rho$  is density,  $C$  is specific heat capacity,  $R$  is the microresonator ring radius,  $d_{r(z)} = \int d_{r(z)} dL / L_{cavity}$  is the halfwidths of fundamental single mode varying along the tapered dispersion-managed microresonator,  $\tau_d = \frac{\pi^{1/3}}{4^{1/3}} \frac{\rho C}{\kappa} d_r^2$ . From 40 kHz to 600 kHz, the measured PSD falls with a 20-dB/decade slope ( $1/f^2$ ) which is quantum-noise limited. The theoretical quantum-noise timing jitter limit without shot-noise is shown in Figure 4c as the orange solid line with the model [55] of

$$S_{\Delta T_R}(f) = \frac{1}{4\pi\sqrt{2}f_R^2} \sqrt{\frac{\gamma}{\Delta_0 D}} \frac{g}{\gamma^2} \left[ \frac{1}{96} \frac{\gamma D}{\Delta_0} \frac{\gamma^2}{f^2} + \frac{1}{24} \left( 1 + \frac{\pi^2 f^2}{\gamma^2} \right)^{-1} \frac{\gamma^2}{f^2} \frac{\Delta_0 D}{\gamma} \right] \quad (3)$$

where  $\gamma$  is the half width half height of the cavity resonance,  $f_R$  is the repetition rate of the microcombs,  $g = \frac{n_2}{n_0} \frac{\hbar \omega_c^2 c}{V_0 n_0}$  is the nonlinear gain coefficient,  $n_0(n_2)$  is the refractive index (nonlinear index) of the nitride resonator,  $\omega_c = 2\pi\nu_c$ ,  $\nu_c$  is the center frequency of the microcombs,  $c$  is the light speed in vacuum,  $V_0$  is the mode volume,  $D = -\frac{\beta_2 \omega_c^2 c}{\gamma n_0}$  is the normalized dispersion and  $\Delta_0 = \omega_0 - \omega_p$  is the resonance-pump detuning. Above the 600 kHz, the measured PSD is limited to be 8905  $\text{zs}^2/\text{Hz}$  by the spectral resolution of the self-heterodyne linear interferometry.

Based on soliton theory, the quantum-noise-limited timing jitter PSD model, especially in the high offset frequency more than 10 kHz, can analytically predict the noise behavior for the mode-locked states via the relation  $S_{\Delta T_R}(f) \approx 0.5294 \frac{\xi}{(2\pi f)^2} \frac{\hbar \nu \alpha_{tot}}{E_p} \frac{\tau_p^2}{T_R}$  [59], where  $E_p \approx \frac{4\pi\hbar\theta\nu_c}{D_1\gamma_c} \sqrt{2D_2\Delta_0}$  is the intracavity pulse energy,  $D_1/2/\pi$  is the cavity FSR,  $D_2$  is related to the group velocity dispersion,  $\theta$  is the transmission of the microresonator,  $\gamma_c$  is the cubic nonlinearity parameter,  $\tau_p \approx \frac{1}{D_1} \sqrt{\frac{D_2}{2\Delta_0}}$  the intracavity pulse duration [45],  $\xi$  and  $\alpha_{tot}$  the spontaneous emission factor and cavity loss. For the different dynamical soliton states, the quantum-noise-limited timing jitter PSD is inversely proportional to the resonance-pump detuning and proportional to square root of the cavity

dispersion. Moreover, the center frequency fluctuation PSD  $S_{\Delta\nu_c}(f)$  of the soliton can be converted into timing jitter with the relation  $S_{\Delta T_R}(f) \approx \left(\frac{D_2}{f T_R}\right)^2 S_{\Delta\nu_c}(f)$  where  $\Delta\nu_c$  is the center frequency fluctuations of the soliton comb triggered by soliton recoil [47], odd-order dispersion [50], or Raman effects [47, 48]. The intracavity intensity fluctuations will also introduce the timing jitter PSD with the relation of  $S_{\Delta T_R}(f) = C \times (\eta P_{in})^2 \left(\frac{1}{f}\right)^2 S_{RIN}(f)$  where the transduction factor of  $\eta = df_R/dP_{in}$ ,  $P_{in}$  is the microresonator intracavity power,  $C$  is a constant [41, 51].

We note our noise measurements on the frequency microcombs below the offset frequency of 20 kHz are still higher than the theoretical microresonator thermodynamical limits attributed to the strong free-running intracavity power fluctuations and pump-resonance detuning noise in the microcomb. Further feedback stabilization of the intracavity power and pump-resonance detuning [41, 48] can improve the timing jitter PSD at the low offset frequency. By increasing tapered waveguide width (increasing the effective resonant mode volume) and decreasing the cavity GVD, the jitter of the frequency DM-microcomb oscillator can be improved to sub-femtosecond timing imprecision.

## Conclusion

In this study the fundamental noise character of dispersion-managed soliton microcombs without a restoring force are examined in detail. A series of dispersion-managed microcombs is generated with a TE-TM dual-driven thermally stabilized technique deterministically and reliably at the single-soliton, double-soliton, and soliton crystal regimes. The RIN is determined to be -153.2 dB/Hz at 100 kHz offset for the single-soliton state and its short-term linewidth is  $\approx 2.3$  kHz at 3.55  $\mu$ s delay time across the span of the individual comb lines, with both parameters bounded by the cw pump laser. The timing jitter PSD is 0.4 as<sup>2</sup>/Hz at 100 kHz offset and the corresponding integrated timing jitter is  $1.7 \pm 0.07$  fs from 10 kHz to 1 MHz. Effective cavity length fluctuation is the main noise source at low offset frequencies, and it originates from intracavity power fluctuations in the microresonator. In the dispersion-managed microcombs, we also note the negligible center frequency shift of the microcomb, preventing center-frequency-shift-related noise conversion processes. Future steps include understanding high-order dispersion in the dispersion-managed microresonators which facilitate additional noise coupling terms. By feedback stabilizing pump laser power and frequency, the timing jitter of the dispersion-managed chip-scale frequency comb oscillator can be further reduced to sub-femtosecond imprecision.

## Methods

**Dispersion-managed microresonator fabrication:** The fabrication procedure of the microresonator starts with a 3  $\mu\text{m}$  thick  $\text{SiO}_2$  layer that is first deposited via plasma-enhanced chemical vapor deposition (PECVD) on a  $p$ -type 8" silicon wafer to serve as the under-cladding oxide. An 800 nm silicon nitride is subsequently deposited via low-pressure chemical vapor deposition (LPCVD) and the resulting nitride layer is patterned by optimized 248 nm deep-ultraviolet lithography and etched down to the buried oxide cladding via an optimized reactive ion etch. The nitride rings are then over-cladded with a 3  $\mu\text{m}$  thick oxide layer, deposited initially with LPCVD for 0.5  $\mu\text{m}$  and then with PECVD for 2.5  $\mu\text{m}$ .

**DM-microcomb numerical modeling:** Taking the anomalous group velocity dispersion (GVD) and mode-crossing-induced frequency shift into consideration, the DM-microcomb formation dynamics is numerically modeled with Lugiato-Lefever equation (LLE) written as:

$$T_R \frac{\partial}{\partial t} A(t, \tau) = \sqrt{\alpha_c} A_p - \left[ \frac{\alpha_c + \alpha_p}{2} + j\delta - j \frac{\beta_2}{2} L_{cav} \frac{\partial^2}{\partial \tau^2} - j \frac{n_2 \omega L_{cav}}{c} I(t, \tau) \right] A(t, \tau)$$

where  $T_R$  is the round-trip time,  $A(t, \tau)$  is the temporal profile of the intracavity field,  $t$  is the slow time corresponding to the evolution time over round trips,  $\tau$  is the fast time describing the temporal structure of the wave,  $A_p$  is the external pump,  $\alpha_p$  is the propagation loss,  $\alpha_c$  is the coupling loss,  $L_{cav}$  is the cavity length, and  $\delta$  is the pump-resonance detuning.  $\beta_2$  describes the second order dispersion coefficient ( $\beta_2 < 0$  indicates anomalous GVD). Here,  $\beta_2$  is chosen to be -4.3  $\text{fs}^2/\text{mm}$ , based on our experimental characterization. To incorporate the mode-crossing-induced frequency shift, an additional frequency shift  $\Delta_n$  is introduced to the  $n$ th mode, so that the mode frequency becomes:  $\omega_n = \omega_0 + D_1 n + \frac{D_2 n^2}{2} + \Delta_n$ .  $\Delta_n$  is determined by the empirical two-parameters model:

$$\frac{\Delta_n}{2\pi} = \frac{-a/2}{n-b-0.5},$$

where  $a$  is the max modal frequency shift,  $n$  and  $b$  are mode number and mode number for max modal frequency shift, respectively.

Thermal effect or Raman effect is not taken account for the simulation. From the dispersion characterization, we estimate  $D_1/2\pi = 88.52$  GHz.

We estimated the maximum frequency shift induced by mode crossing to be  $\frac{\Delta_n}{2\pi} = 130$  MHz at 1581.5 nm based on the soliton recoil spectral peak. The estimated value is supported by comparing the simulated comb spectrum with the experimental result, which are in good qualitative agreement. 2,001 modes centered at the pump are incorporated in the LLE modeling.

The simulation starts from vacuum noise and run for  $1 \times 10^5$  roundtrips until the solution reaches steady state. The modeled soliton crystal state ( $\delta = 0.044$ ), double-soliton state ( $\delta = 0.058$ ), and single-soliton state ( $\delta = 0.062$ ) are obtained with the same initial parameters but different noise input.

**Relative intensity noise and Short-time delayed linear interferometry:** The filtered microcombs without pump laser is injected into a photodetector (Thorlabs PDA10CF) with optical power of 210  $\mu\text{W}$ . A multimeter and an oscilloscope monitor the DC voltage ( $V_0$ ) and a signal source analyzer (Keysight E5052B) records the voltage fluctuation PSD  $S_{\Delta I}(f)$ . One of soliton microcomb modes is selected by a 230 pm diffractive grating based tunable optical filter (JDS Uniphase TB9) and this mode is sent into the SDLI to obtain the coherent envelopes with different delay time. The coherent envelopes were recorded by an electrical spectrum analyzer (Agilent CXA N9000A) with resolution bandwidth of 10 Hz and a span of 2 MHz, averaged over 50 scans. The input power of SDLI is 500  $\mu\text{W}$ .

**Self-heterodyne linear interferometry:** A home-build diffractive grating pair is used to select the modes for the timing jitter PSD measurement. We first optimize the noise floor of the HLI by improving the signal-to-noise ratio of the detected RF signal at 100 MHz. Secondly, we minimize the relative delay time between the two optical modes ( $\nu_n = 190.11$  THz,  $\nu_m = 192.55$  THz) and power difference of the two arms of HLI, to enable the suppression of the common-mode noise. Thirdly, we optimize the delay time for the soliton microcomb based on two criteria. One criterion is to maximize the timing jitter measurement sensitivity and the other is to expand the measured Fourier offset frequency range. The fiber delay length was optimized to be 49 m. The detected RF signals at the output of the two PD are at 14 and 19 dBm.

## References

1. S. A. Diddams, K. Vahala, and T. Udem, Optical frequency combs: Coherently uniting the electromagnetic spectrum. *Science* **369**, 267 (2020).
2. T. Udem, R. Holzwarth, and T. W. Hansch, Optical frequency metrology. *Nature* **416**, 233-236 (2002).
3. M. Lezius, T. Wilken, C. Deutsch, M. Giunta, O. Mandel, A. Thaller, V. Schkolnik, M. Schiemangk, A. Dinkelaker, A. Kohfeldt, A. Wicht, M. Krutzik, A. Peters, O. Hellmig, H.

- Duncker, K. Sengstock, P. Windpassinger, K. Lampmann, T. Hulsing, T. W. Hansch, and R. Holzwarth, Space-borne frequency comb metrology. *Optica* **3**, 1381–1386 (2016).
4. J. Lee, K. Lee, Y.-S. Jang, H. Jang, S. Han, S.-H. Lee, K.-I. Kang, C.-W. Lim, Y.-J. Kim, and S.-W. Kim, Testing of a femtosecond pulse laser in outer space. *Sci. Rep.* **4**, 5134-5137 (2014).
  5. I. Coddington, W. C. Swann, L. Nenadovic, and N. R. Newbury, Rapid and precise absolute distance measurements at long range. *Nat. Photon* **3**, 351–356 (2009).
  6. T. M. Fortier, M. S. Kirchner, F. Quinlan, J. Taylor, J. C. Bergquist, T. Rosenband, N. Lemke, A. Ludlow, Y. Jiang, C. W. Oates, and S. A. Diddams, Generation of ultrastable microwaves via optical frequency division. *Nat. Photon* **5**, 425–429 (2011).
  7. X. Xie, R. Bouchand, D. Nicolodi, M. Giunta, W. Hänsel, M. Lezius, A. Joshi, S. Datta, C. Alexandre, M. Lours, P. Tremblin, G. Santarelli, R. Holzwarth, and Y. L. Coq, Photonic microwave signals with zeptosecond-level absolute timing noise. *Nat. Photon* **11**, 44–47 (2017).
  8. T. J. Kippenberg, A. L. Gaeta, M. Lipson, and M. L. Gorodetsky, Dissipative Kerr solitons in optical microresonators. *Science* **361**, 8083 (2018).
  9. T. Herr, V. Brasch, J. D. Jost, C. Y. Wang, N. M. Kondratiev, M. L. Gorodetsky, and T. J. Kippenberg, Temporal solitons in optical microresonators. *Nat. Photon* **8**, 145–152 (2014).
  10. A. Tikan, J. Riemensberger, K. Komagata, S. Hönl, M. Churayev, C. Skehan, H. Guo, R. N. Wang, J. Liu, P. Seidler, and T. J. Kippenberg, Emergent nonlinear phenomena in a driven dissipative photonic dimer. *Nat. Phys.* (2021).
  11. V. Brasch, M. Geiselmann, T. Herr, G. Lihachev, M. H. P. Pfeiffer, M. L. Gorodetsky, and T. J. Kippenberg, Photonic chip-based optical frequency comb using soliton Cherenkov radiation. *Science* **351**, 357–360 (2016).
  12. J. Q. Liu, E. Lucas, A. S. Raja, J. J. He, J. Riemensberger, R. N. Wang, M. Karpov, H. R. Guo, R. Bouchand, and T. J. Kippenberg, Photonic microwave generation in the X- and K-band using integrated soliton microcombs. *Nat. Photonics* **14**, 486–491 (2020).
  13. Z. Gong, A. Bruch, M. Shen, X. Guo, H. Jung, L. Fan, X. W. Liu, L. Zhang, J. X. Wang, J. M. Li, J. C. Yan, and H. X. Tang, High-fidelity cavity soliton generation in crystalline AlN micro-ring resonators. *Opt. Lett.* **43**, 4366–4369 (2018).

14. Y. He, Q.-F. Yang, J. W. Ling, R. Luo, H. X. Liang, M. X. Li, B. Q. Shen, H. M. Wang, K. Vahala, and Q. Lin, Self-starting bi-chromatic LiNbO<sub>3</sub> soliton microcomb. *Optica* **6**, 1138–1144 (2019).
15. L. Chang, W. Q. Xie, H. W. Shu, Q.-F. Yang, B. Q. Shen, A. Boes, J. D. Peters, W. Jin, C. Xiang, S. T. Liu, G. Moille, S.-P. Yu, X. J. Wang, K. Srinivasan, S. B. Papp, K. Vahala, and J. E. Bowers, Ultra-efficient frequency comb generation in AlGaAs-on-insulator microresonators. *Nature Commun.* **9**, 1869 (2018).
16. X. X. Xue, Y. Xuan, Y. Liu, P. H. Wang, S. Chen, J. Wang, D. E. Leaird, M. H. Qi, and A. M. Weiner, Mode-locked dark pulse Kerr combs in normal-dispersion microresonators. *Nat. Photonics* **9**, 594–600 (2015).
17. S. W. Huang, H. Zhou, J. H. Yang, J. F. McMillan, A. Matsko, M. Yu, D. L. Kwong, L. Maleki, and C. W. Wong, Mode-locked ultrashort pulse generation from on-chip normal dispersion microresonators. *Phys. Rev. Lett.* **114**, 053901 (2015).
18. H. Liu, S.-W. Huang, J. Yang, M. Yu, D.-L. Kwong, and C. W. Wong, Bright square pulse generation by pump modulation in a normal GVD microresonator. In: Conference on Lasers and Electro-Optics. OSA: Washington, D.C., 2017, p FTu3D.3.
19. H. Wang, B. Shen, L. Wu, C. Bao, W. Jin, L. Chang, M. A. Leal, A. Feshali, M. Paniccia, J. E. Bowers, and K. Vahala, Self-regulating soliton domain walls in microresonators. 2021.<http://arxiv.org/abs/2103.10422> (accessed 22 Mar2021).
20. G. Lihachev, J. Liu, W. Weng, L. Chang, J. Guo, J. He, R. N. Wang, M. H. Anderson, J. E. Bowers, and T. J. Kippenberg, Platicon microcomb generation using laser self-injection locking. 2021.<http://arxiv.org/abs/2103.07795> (accessed 19 Mar2021).
21. Ó. B. Helgason, F. R. Arteaga-Sierra, Z. C. Ye, K. Twayana, P. A. Andrekson, M. Karlsson, J. Schröder, and V. Torres-Company, Dissipative solitons in photonic molecules. *Nat. Photonics* **15**, 305–310 (2021).
22. B. Stern, X. C. Ji, Y. Okawachi, A. L. Gaeta, and M. Lipson, Battery-operated integrated frequency comb generator. *Nature* **562**, 401–415 (2018).
23. A. S. Raja, A. S. Voloshin, H. R. Guo, S. E. Agafonova, J. Q. Liu, A. S. Gorodnitskiy, M. Karpov, N. G. Pavlov, E. Lucas, R. R. Galiev, A. E. Shitikov, J. D. Jost, M. L. Gorodetsky, and T. J. Kippenberg, Electrically pumped photonic integrated soliton microcomb. *Nat. Commun.* **10**, 680 (2019); correction **10**, 1623 (2019).

24. B. Q. Shen, L. Chang, J. Q. Liu, H. M. Wang, Q.-F. Yang, C. Xiang, R. N. Wang, J. J. He, T. Y. Liu, W. Q. Xie, J. Guo, D. Kinghorn, L. Wu, Q.-X. Ji, T. J. Kippenberg, K. Vahala, and J. E. Bowers, Integrated turnkey soliton microcombs. *Nature* **582**, 365–369 (2020).
25. W. Jin, Q.-F. Yang, L. Chang, B. Q. Shen, H. M. Wang, M. A. Leal, L. Wu, M. D. Gao, A. Feshali, M. Paniccia, K. J. Vahala, and J. E. Bowers, Hertz-linewidth semiconductor lasers using CMOS-ready ultrahigh-Q microresonators. *Nat. Photonics* **15**, 1–8 (2021).
26. P. Marin-Palomo, J. N. Kemal, M. Karpov, A. Kordts, J. Pfeifle, M. H. P. Pfeiffer, P. Trocha, S. Wolf, V. Brasch, M. H. Anderson, R. Rosenberger, K. Vijayan, W. Freude, T. J. Kippenburg, and C. Koos, Microresonator-based solitons for massively parallel coherent optical communications. *Nature* **546**, 274-279 (2017).
27. A. Fülöp, M. Mazur, A. Lorences-Riesgo, Ó. B. Helgason, P.-H. Wang, Y. Xuan, D. E. Leaird, M. H. Qi, and P. A. Andrekson, A. M. Weiner, and V. Torres-Company, High-order coherent communications using mode-locked dark-pulse Kerr combs from microresonators. *Nat. Commun.* **9**, 1598 (2018).
28. B. Corcoran, M. X. Tan, X. Y. Xu, A. Boes, J. Y. Wu, T. G. Nguyen, S. T. Chu, B. E. Little, R. Morandotti, A. Mitchell, and D. J. Moss, Ultra-dense optical data transmission over standard fibre with a single chip source. *Nat. Commun.* **11**, 2568 (2020).
29. J. Riemensberger, A. Lukashchuk, M. Karpov, W. L. Weng, E. Lucas, J. Q. Liu, and T. J. Kippenberg, Massively parallel coherent laser ranging using a soliton microcomb. *Nature* **581**, 164-170 (2020).
30. S.-W. Huang, J. H. Yang, M. Yu, B. H. McGuyer, D.-L. Kwong, T. Zelevinsky, and C. W. Wong, A broadband chip-scale optical frequency synthesizer at  $2.7 \times 10^{-16}$  relative inaccuracy. *Sci. Adv.* **2**, e1501489 (2016).
31. D. T. Spencer, T. Drake, T. C. Briles, J. Stone, L. C. Sinclair, C. Fredrick, Q. Li, D. Westly, B. R. Ilic, A. Bluestone, N. Volet, T. Komljenovic, L. Chang, S. H. Lee, D. Y. Oh, M. G. Suh, K. Y. Yang, M. P. Pfeiffer, T. J. Kippenberg, E. Norberg, L. Theogarajan, K. Vahala, N. R. Newbury, K. Srinivasan, J. E. Bowers, S. A. Diddams, and S. B. Papp, An optical-frequency synthesizer using integrated photonics. *Nature* **557**, 81-85 (2018).
32. E. Obrzud, M. Rainer, A. Harutyunyan, M. H. Anderson, M. Geiselmann, B. Chazelas, S. Kundermann, S. Lecomte, M. Cecconi, A. Ghedina, E. Molinari, F. Pepe, F. Wildi, F. Bouchy, T. J. Kippenberg, and T. Herr, A microphotonic astrocomb. *Nat. Photonics* **13**, 31–35 (2019).



33. M. G. Suh, X. Yi, Y.-H. Lai, S. Leifer, I. S. Grudinin, G. Vasisht, E. C. Martin, M. P. Fitzgerald, G. Doppmann, J. Wang, D. Mawet, S. B. Papp, S. A. Diddams, C. Beichman, and K. J. Vahala, Searching for exoplanets using a microresonator astrocomb. *Nat. Photonics* **13**, 25–30 (2019).
34. M. G. Suh, Q.-F. Yang, K. Y. Yang, X. Yi, and K. J. Vahala, Microresonator soliton dual-comb spectroscopy. *Science* **354**, 600-603 (2016).
35. A. Dutt, C. Joshi, X. C. Ji, J. Cardenas, Y. Okawachi, K. Luke, A. L. Gaeta, and M. Lipson, On-chip dual-comb source for spectroscopy. *Sci. Adv.* **2**, e1701858 (2018).
36. M. J. Yu, Y. Okawachi, A. G. Griffith, N. Picqué, M. Lipson, and A. L. Gaeta, Solicon-chip-based mid-infrared dual-comb spectroscopy. *Nat. Commun.* **9**, 1869 (2018).
37. Y-S. Jang, H. Liu, J. H. Yang, M. B. Yu, D. L. Kwong, and C. W. Wong, Nanometric precision distance metrology via hybrid spectrally-resolved and homodyne interferometry in a single-soliton frequency microcomb. *Phys. Rev. Lett.* **126**, 023903 (2021).
38. M. G. Suh and K. J. Vahala, Soliton microcomb range measurement. *Science* **359**, 884-887 (2018).
39. P. Trocha, M. Karpov, D. Ganin, M. H. P. Pfeiffer, A. Kordts, S. Wolf, J. Krockenberger, P. M. Palomo, C. Weimann, S. Randel, W. Freude, T. J. Kippenberg, and C. Koos, Ultrafast optical ranging using microresonator soliton frequency combs. *Science* **359**, 887-891 (2018).
40. W. Liang, D. Eliyahu, V. S. Ilchenko, A. A. Savchenkov, A. B. Matsko, D. Seidel, and L. Maleki, High spectral purity Kerr frequency comb radio frequency photonic oscillator. *Nat. Commun.* **6**, 7957 (2015).
41. E. Lucas, P. Brochard, R. Bouchand, S. Schilt, T. Südmeyer, and T. J. Kippenberg, Ultralow-noise photonic microwave synthesis using a soliton microcomb-based transfer oscillator. *Nat. Commun.* **11**, 374 (2020).
42. D. Jeong, D. Kwon, I. Jeon, I. H. Do, J. Kim, and H. Lee, Ultralow jitter silica microcomb. *Optica* **7**, 1108 (2020).
43. J. Feldmann, N. Youngblood, M. Karpov, H. Gehring, X. Li, M. Stappers, M. Le Gallo, X. Fu, A. Lukashchuk, A. S. Raja, J. Liu, C. D. Wright, A. Sebastian, T. J. Kippenberg, W. H. P. Pernice, and H. Bhaskaran, Parallel convolutional processing using an integrated photonic tensor core. *Nature* **589**, 52-58 (2021).

44. X. Y. Xu, M. X. Tan, B. Corcoran, J. Y. Wu, A. Boes, T. G. Nguyen, S. T. Chu, B. E. Little, D. G. Hicks, R. Morandotti, A. Mitchell, and D. J. Moss, 11 TOPS photonic convolutional accelerator for optical neural networks. *Nature* **589**, 44-51 (2021).
45. E. Lucas, H. R. Guo, J. D. Jost, M. Karpov, and T. J. Kippenberg, Detuning-dependent properties and dispersion-induced instabilities of temporal dissipative Kerr solitons in optical microresonators. *Phys. Rev. A* **95**, 043822 (2017).
46. J. R. Stone, T. C. Briles, T. E. Drake, D. T. Spencer, D. R. Carlson, S. A. Diddams, and S. B. Papp, Thermal and nonlinear dissipative-soliton dynamics in Kerr-microresonator frequency combs. *Phys. Rev. Lett.* **121**, 063902 (2018).
47. X. Yi, Q. F. Yang, X. Zhang, K. Y. Yang, X. Li, and K. Vahala, Single-mode dispersive waves and soliton microcomb dynamics. *Nat. Commun.* **8**, 14869 (2017).
48. Q.-F. Yang, Q.-X. Ji, L. Wu, B. Shen, H. Wang, C. Bao, Z. Yuan, and K. Vahala, Dispersive-wave induced noise limits in miniature soliton microwave sources. *Nat. Commun.* **12**, 1442 (2021).
49. Y. Bai, M. H. Zhang, Q. Shi, S. Ding, Y. Qin, Z. Xie, X. Jiang, and M. Xiao, Brillouin-Kerr Soliton Frequency Combs in an Optical Microresonator. *Phys. Rev. Lett.* **126**, 063901 (2021).
50. J. R. Stone, and S. B. Papp, Harnessing dispersion in soliton microcombs to mitigate thermal noise. *Phys. Rev. Lett.* **125**, 153901 (2020).
51. T. E. Drake, J. R. Stone, T. C. Briles, and S. B. Papp, Thermal decoherence and laser cooling of Kerr microresonator solitons. *Nat. Photonics.* **14**, 480–485 (2020).
52. C. Bao, M.-G. Suh, B. Shen, K. Şafak, A. Dai, H. Wang, L. Wu, Z. Yuan, Q.-F. Yang, A. B. Matsko, F. X. Kärtner, and K. J. Vahala, Quantum diffusion of microcavity solitons. *Nat. Phys.* **17**, 462-466 (2021).
53. K. Jia, X. Wang, D. Kwon, J. Wang, E. Tsao, H. Liu, X. Ni, J. Guo, M. Yang, X. Jiang, J. Kim, S.-N. Zhu, Z. Xie, and S.-W. Huang, Photonic flywheel in a monolithic fiber resonator. *Phys. Rev. Lett.* **125**, 143902 (2020).
54. Y. Li, S.-W. Huang, B. Li, H. Liu, J. Yang, A. K. Vinod, K. Wang, M. Yu, D.-L. Kwong, H.-T. Wang, K. K.-Y. Wong, and C. W. Wong, Real-time transition dynamics and stability of chip-scale dispersion-managed frequency microcombs. *Light Sci. Appl.* **9**, 52 (2020).
55. A. B. Matsko and L. Maleki, On timing jitter of mode-locked Kerr frequency combs. *Opt. Express* **21**, 28862-28876 (2013).

56. D. Kwon, C. G. Jeon, J. Shin, M. S. Heo, S. E. Park, Y. J. Song, and J. W. Kim, Reference-free, high-resolution measurement method of timing jitter spectra of optical frequency combs. *Sci. Rep.* **7**, 40917 (2017).
57. S. H. Huang, T. Zhu, M. Liu, and W. Huang, Precise measurement of ultra-narrow laser linewidths using the strong coherent envelope. *Sci. Rep.* **7**, 41988 (2016).
58. G. Huang, E. Lucas, J. Liu, A. S. Raja, G. Lihachev, M. L. Gorodetsky, N. J. Engelsen, and T. J. Kippenberg, Thermorefractive noise in silicon-nitride microresonators. *Phys. Rev. A* **99**, 061801 (2019).
59. R. Paschotta, Noise of mode-locked lasers (Part II): timing jitter and other fluctuations. *Appl. Phys. B* **79**, 163-173 (2004).

### **Acknowledgements**

The authors acknowledge fruitful discussions with Prof. Shu-Wei Huang, Scott Diddams, Tara Drake, and Dohyeon Kwon on the measurements, with Prof. Guo Qing Chang and Prof. Ming Xin on noise theory, and with Prof. Ken Yang. We acknowledge financial support from the Lawrence Livermore National Laboratory (B622827), the National Science Foundation (1824568, 1810506, 1741707, 1829071), and the Office of Naval Research (N00014-16-1-2094).

### **Author contributions**

W.W. and H.L. conducted the experiments. W.W. analyzed the data and performed the simulations. J.Y. designed the microresonator. J.Y., A.K.V. J.L. and Y.S.J. contributed to the design of the experiments. H.Z. contributed to the simulations. M.Y. and D.-L.K. performed the device nanofabrication. W.W., J.Y., P.D., J.C., and C.W.W. initiated the project. W.W., and C.W.W. wrote the manuscript. All authors discussed the results.

### **Author Information**

Reprints and permissions information is available at [www.nature.com/reprints](http://www.nature.com/reprints). The authors declare no competing interests. Readers are welcome to comment on the online version of the paper. Correspondence and requests for materials should be addressed to W.W. and C.W.W. ([wentingwang@ucla.edu](mailto:wentingwang@ucla.edu); [cheewei.wong@ucla.edu](mailto:cheewei.wong@ucla.edu)).

### **Supplementary Information**

Supplementary information is available in the online version of the paper. Reprints and permissions information is available online at [www.nature.com/reprints](http://www.nature.com/reprints).

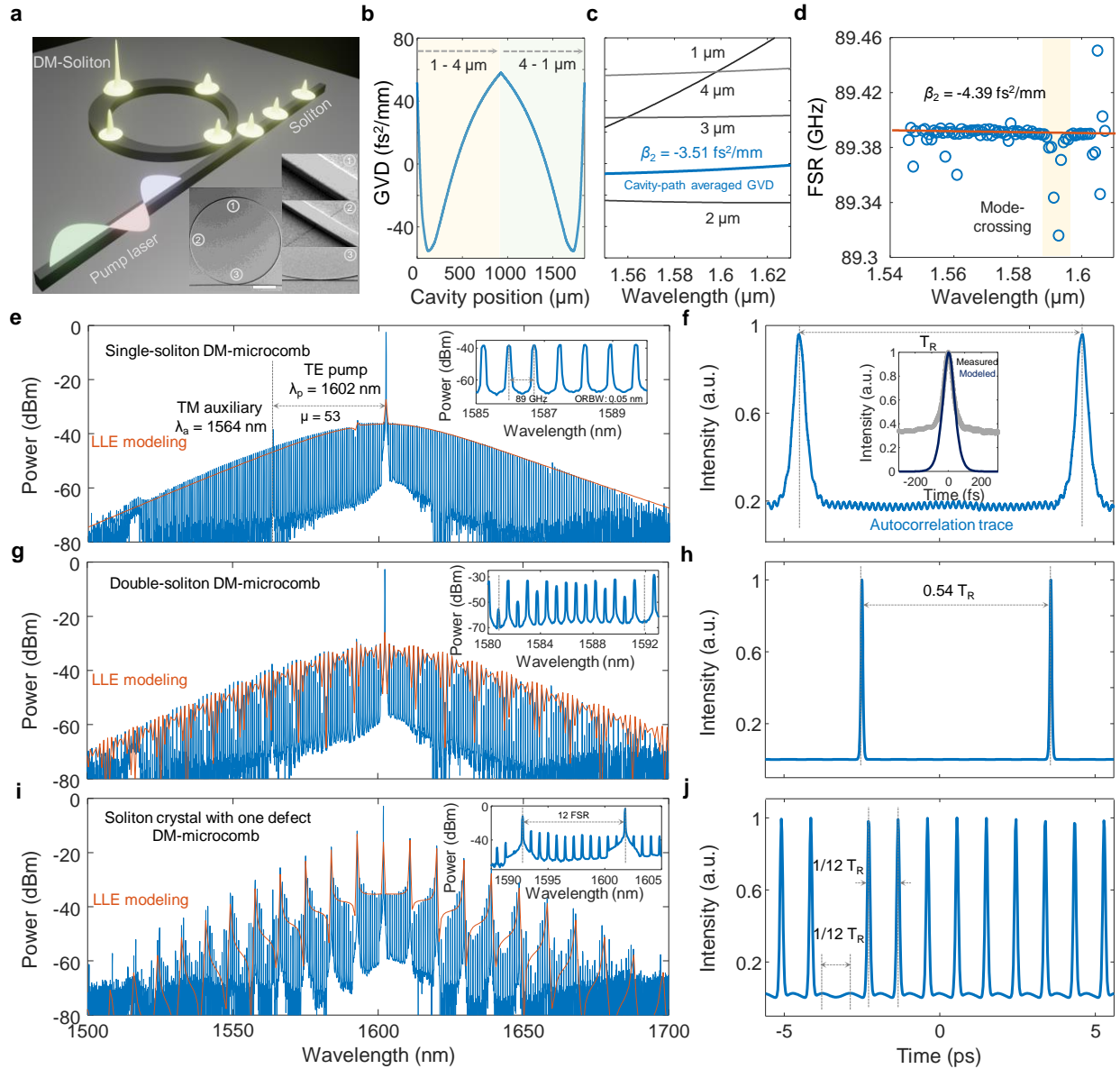


**Figure 1 | Soliton microcomb formation in tapered dispersion-managed microresonators. a**, Schematic illustration of dispersion-managed (DM) soliton microcombs generation. Inset: scanning electron microscope of the microresonator and the zoomed waveguide and coupling gap. Scale bar: 130  $\mu\text{m}$ . **b**, Correspondingly calculated group velocity dispersion (GVD) variation along the microresonator. **c**, Calculated GVD of different waveguide widths at a fixed waveguide height, and the corresponding cavity-path averaged GVD. **d**, Measured GVD via swept-wavelength

interferometry with  $\beta_2 = -4.39 \text{ fs}^2/\text{mm}$ . **e**, **g**, and **i**, Measured optical spectra of the single-soliton, double-soliton and soliton crystal with one defect DM-microcomb. The Lugiato-Lefever equation (LLE) modeling is also plotted, with the negligible center frequency shift (detailed in Supplementary Information II). Insets are the zoomed optical spectra. **f**, Measured intensity autocorrelation trace of the single-soliton DM-microcomb. Inset is the measured and modeled pulse duration. **h**, Modeled intracavity waveform of the double-soliton with a temporal separation of  $0.54 \times T_R$ . **j**, Modeled intracavity waveform of the soliton crystal with one defect showing the modulated background (“potential well”) with a period of  $1/12 \times T_R$ .

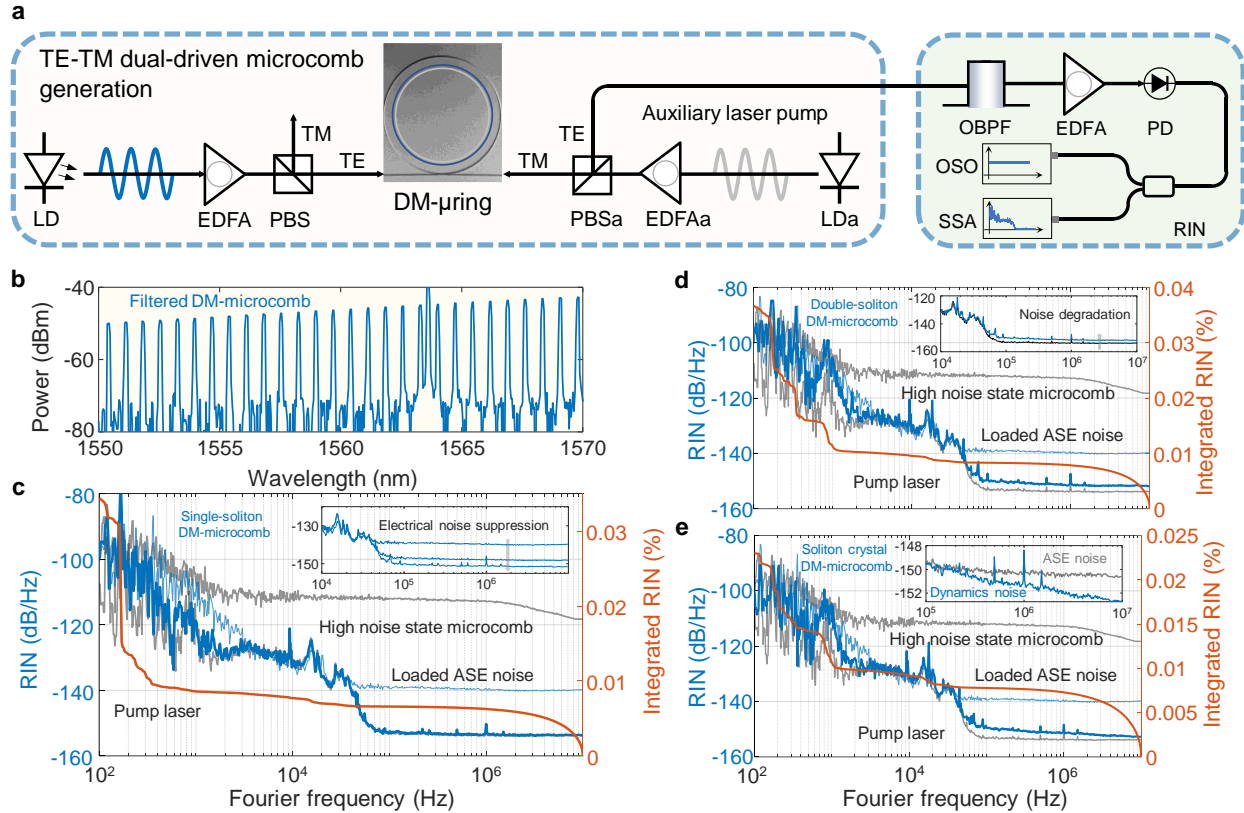


**Figure 2 | Relative intensity noise (RIN) measurements of the dispersion-managed microcombs.** **a**, Experimental setup of the TE-TM dual-driven approach for the thermally stabilized soliton microcomb generation and the relative intensity noise measurement. LD: laser diode; EDFA: erbium-doped fiber amplifier; PBS: polarization beam splitter; TE: transverse-electric polarization; TM: transverse-magnetic polarization, OBPF: optical bandpass filter; PD: photodiode; OSO: oscilloscope; SSA: signal source analyzer. **b**, Representatively filtered optical spectrum of the single-soliton DM microcomb. **c**, **d**, and **e**, Relative intensity noise power spectral density (PSD) and the corresponding integrated RIN of the microcombs at the different dynamical states along with the lower bound set by the pump laser. The RIN PSD of the chaotic DM-microcomb and the RIN PSD after loading broadband ASE noise are also illustrated. Inset of **c**: Electrical noise optimization by adjusting the incident optical power of the PD to explore the soliton dynamical intensity fluctuations at the different dynamical states. Inset of **d**: Noise degradation of the double-soliton DM-microcomb showing the additional white high-frequency noise. Inset of **e**: Noise degradation of the soliton crystal DM-microcomb showing the dynamical high-frequency noise.

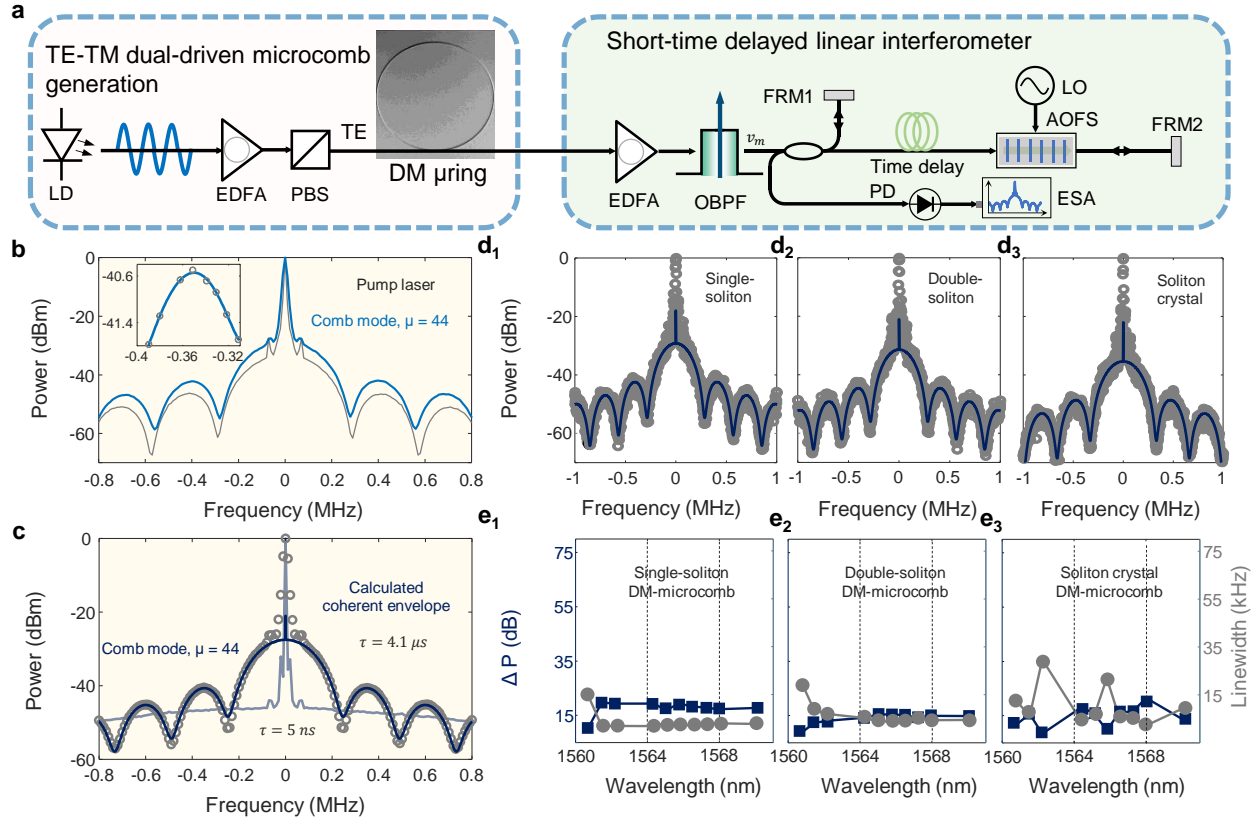


**Figure 3 | Near-instantaneous linewidth measurement of the DM-microcomb.** **a**, Experimental setup of the short-time delayed linear interferometer (SDLI). FRM: Faraday rotator mirror, AOFS: acoustic optical frequency shifter, LO: local oscillator, ESA: electrical spectrum analyzer. **b**, Measured interferometric coherence envelope (ICE) of the pump laser and one of DM-microcomb lines ( $\mu = 44$ ). Inset is the peak detection based on polynomial curve fitting. **c**, Measured ICE with the different time delays to show the spectral resolution and power dynamic range of the SDLI. **d<sub>1</sub>**, **d<sub>2</sub>**, and **d<sub>3</sub>**, Measured ICE of one of comb line of the single-soliton, double-soliton and soliton crystal DM microcombs. **e<sub>1</sub>**, **e<sub>2</sub>**, and **e<sub>3</sub>**, Linewidth distributions of the different comb lines from 1560 nm to 1570 nm, for the varied soliton comb states. Pump is at 1602 nm.

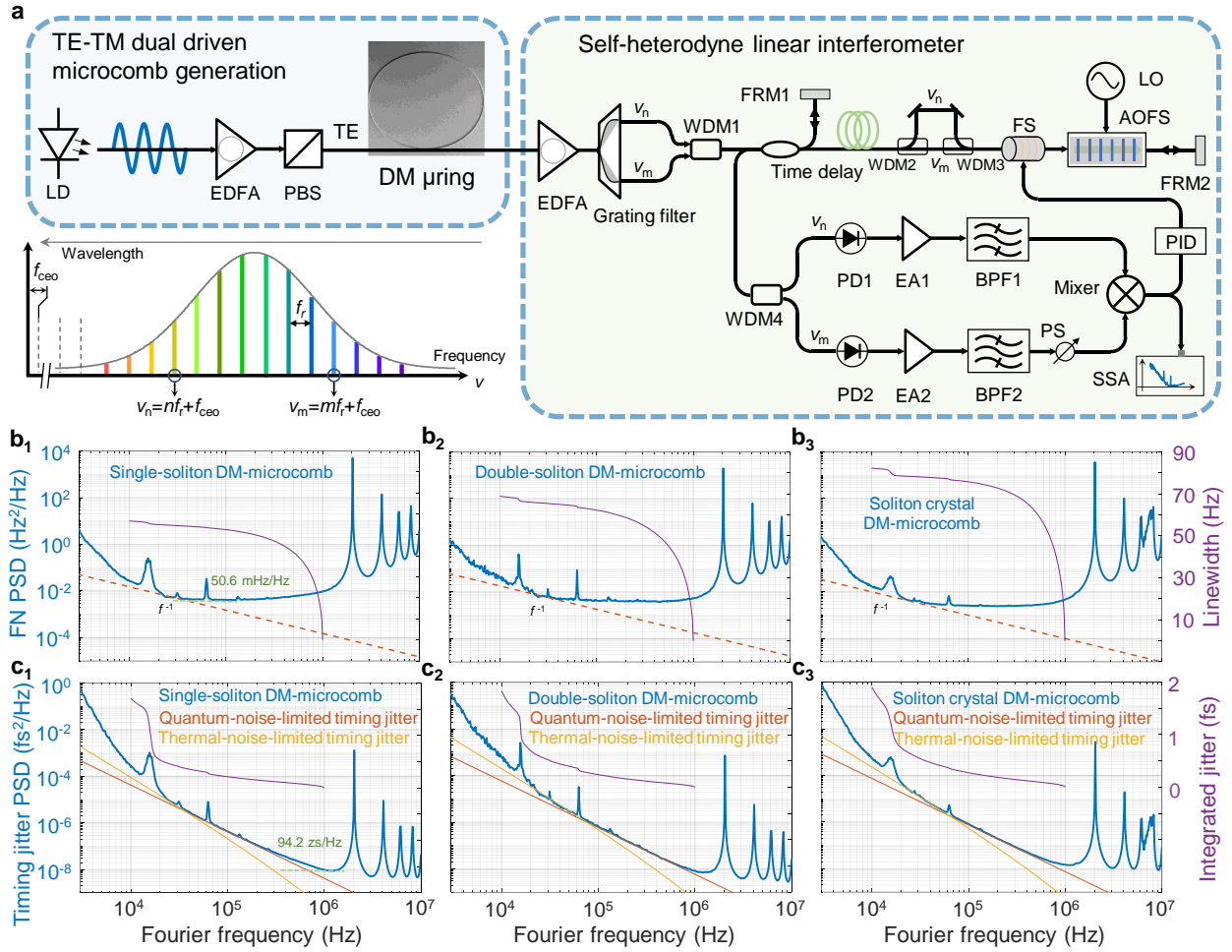


**Figure 4 | Measured repetition rate frequency noise PSD and timing jitter PSD and the correspondingly integrated RF linewidth and timing jitter of the dispersion-managed soliton microcombs.** **a**, Experimental setup of the self-heterodyne linear interferometer (HLI). WDM: wavelength division multiplexer; FS: fiber stretcher; EA: electronic amplifier; BPF: bandpass filter, PS: phase shifter; PID: proportional-integral-differential controller. Inset is the schematic illustration of the self-heterodyne linear interferometry. **b<sub>1</sub>**, **b<sub>2</sub>**, and **b<sub>3</sub>**, Measured frequency noise PSD at the different soliton states with a 49-m stabilized fiber link. The orange dashed line denotes a 10-dB/decade slope indicating a frequency free-walk induced by the intracavity power fluctuations of the microresonator. The corresponding repetition rate tone linewidth integrated from 1 MHz to 10 kHz is denoted with purple curves. **c<sub>1</sub>**, **c<sub>2</sub>**, and **c<sub>3</sub>**, Timing jitter PSD measurement of the soliton microcombs at different dynamical states with the calculated thermal noise and quantum noise limits. The timing jitter theoretical models are from Ref. 55 and Ref. 58 denoting



with the solid orange and yellow lines as the quantum-noise limit and thermal-noise limit of the soliton microcombs. The correspondingly integrated timing jitter is included.